3D Radial Projection Technique With Ultrashort Echo Times for Sodium MRI: Clinical Applications in Human Brain and Skeletal Muscle

Sònia Nielles-Vallespin,[1,2*] Marc-André Weber,[3] Michael Bock,[1] André Bongers,[1] Peter Speier,[2] Stephanie E. Combs,[4] Johannes Wöhrle,[5] Frank Lehmann-Horn,[6] Marco Essig,[3] and Lothar R. Schad[1]

^{23}Na MRI has the potential to noninvasively detect sodium (Na) content changes in vivo. The goal of this study was to implement ^{23}Na MRI in a clinical setting for neurooncological and muscular imaging. Due to the biexponential T_2 decay of the tissue Na signal with a short component, which ranges between 0.5–8 ms, the measurement of total Na content requires imaging techniques with echo times (TEs) below 0.5 ms. A 3D radial pulse sequence with a TE of 0.2 ms at a spatial resolution of 4 × 4 × 4 mm^3 was developed that allows the acquisition and presentation of Na images on the scanner. This sequence was evaluated in patients with low- and high-grade gliomas, and higher ^{23}Na MR signals corresponding to an increased Na content were found in the tumor regions. The contrast-to-noise ratio (CNR) between tumor and white matter increased from 0.8 ± 0.2 to 1.3 ± 0.3 with tumor grade. In patients with an identified muscular ^{23}Na channelopathy (Paramyotonia congenita (PC)), induced muscle weakness led to a signal increase of ~18% in the ^{23}Na MR images, which was attributed to intracellular Na^+ accumulation in this region. Magn Reson Med 57: 74–81, 2007. © 2006 Wiley-Liss, Inc.

Key words: sodium magnetic resonance imaging; tissue viability; image reconstruction; MR pulse sequence; glioma; paramyotonia congenita

Sodium (Na) ions play a vital role in cellular homeostasis and electrochemical activity throughout the human body. The rationale for investigating Na changes relates to the Na concentration gradient, which exists between intra- and extracellular environments. This concentration gradient consists of an approximately 10-fold Na concentration difference in the extracellular space with an Na concentration of $[Na^+]_{ex}$ = 145 mM relative to the intracellular space with $[Na^+]_{in}$ = 10–15 mM (1). The total Na concentration visualized by ^{23}Na MRI reflects the volume-weighted mean of these two compartments. Under pathological conditions the Na gradient between intra- and extracellular space is altered, and an elevated Na concentration due to an increased $[Na^+]_{in}$ is often observed (2). An increased ^{23}Na MR signal related to increased $[Na^+]_{in}$ has been observed in brain tumors (2), ischemic heart disease (3,4), and skeletal myopathies (5,6).

Na has a spin 3/2 nucleus with three degenerate single-quantum ($\Delta m = 1$) energy transitions between the four Zeeman levels. Additionally, Na exhibits an electric quadrupole moment that distorts the otherwise spherical distribution of charge about the nucleus. The interactions between the electric quadrupole moment and the electric field gradient of the environment lift the degeneracy of the three transitions (7–11). In biological tissue this line-splitting is averaged out over time, and the ^{23}Na MR signal decays with two distinct T_2 relaxation times: a slow component (T_{2s}) of 15–30 ms, and a fast component (T_{2f}) of 0.5–8 ms (6). However, the in vivo detection of Na by MRI is hindered by fast transverse relaxation, low tissue-equivalent concentrations, and the small gyromagnetic ratio of Na ions compared to standard proton ^{1}H MRI (12,13).

Na MR studies may be classified into three main groups: paramagnetic shift reagents (14), multiple-quantum filtering (15), and ^{23}Na MRI of the total Na content (16–18). Shift reagents allow discrimination between intra- and extracellular Na; however, these are restricted to animal experiments due to the toxicity of the available ^{23}Na shift reagents (14). Multiple-quantum filtering techniques can distinguish between T_{2s} and T_{2f} Na fractions, but suffer from even lower SNR than conventional imaging studies (15). In order to detect both T_2 components, imaging techniques with ultrashort TEs of less than 500 μs are required (16–18). Both 3D radial techniques (16) and twisted projection imaging (TPI) (17,18) with TE = 400 μs have been successfully used in brain studies (2), musculoskeletal imaging (6), and heart studies (4). In these cases, where TE is less than 500 microseconds, the image intensity is proportional to the Na^+ content, which is a weighted average of $[Na^+]_{ex}$ and $[Na^+]_{in}$.

For a compartment (x) the Na^+ concentration $[Na^+]_x$ = $Na^+{}_x$ content/Volume$_x$; therefore, the Na^+ NMR content ($Na^+{}_x$ content = $[Na+]_x$ * Volume$_x$) measurement (spectroscopic or imaging) will be a function of changes in the Na^+ concentration and/or volume. Ultrashort TE (UTE) Na^+ imaging techniques measure the total Na^+ content = $[Na^+]_{in}$ * Volume$_{in}$ +$[Na^+]_{ex}$ * Volume$_{ex}$. Despite the inability of UTE methods to resolve intra- and extracellular

[1]Medical Physics in Radiology, Deutsches Krebsforschungszentrum, Heidelberg, Germany.

[2]Siemens Medical Solutions, Erlangen, Germany.

[3]Department of Radiology, Deutsches Krebsforschungszentrum, Heidelberg, Germany.

[4]Clinical Cooperation Unit Radiotherapeutical Oncology, Deutsches Krebsforschungszentrum, Heidelberg, Germany.

[5]Department of Neurology, University Hospital Mannheim, Mannheim, Germany.

[6]Department of Applied Physiology, University of Ulm, Ulm, Germany.

Grant sponsor: Deutsche Forschungsgemeinschaft; Grant number: Scha 546/11-1; Grant sponsor: Medical School Research Council, University of Heidelberg; Grant number: 196/2002.

*Correspondence to: Sonia Nielles-Vallespin, Siemens AG Medical Solutions, MREA-CV, Karl-Schall-Str. 6, 91052 Erlangen, Germany. E-mail: sonia.nielles-vallespin@siemens.com

Received 10 August 2005; revised 20 July 2006; accepted 29 August 2006.
DOI 10.1002/mrm.21104
Published online in Wiley InterScience (www.interscience.wiley.com).

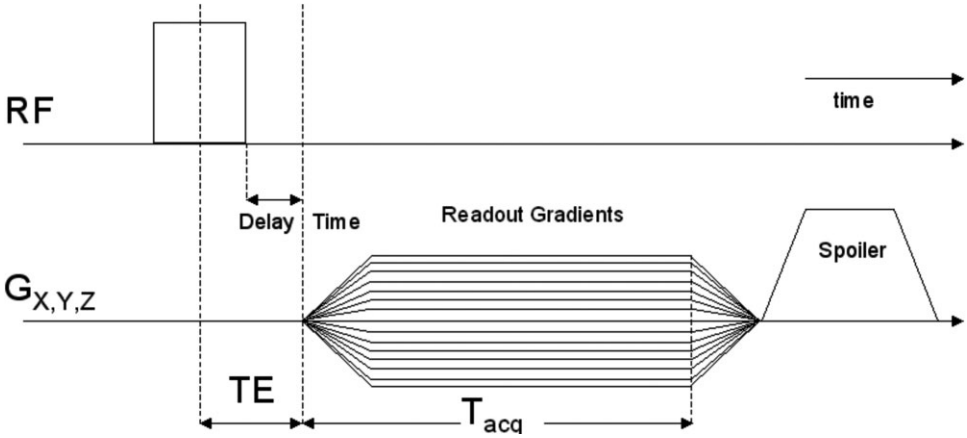

FIG. 1. 3D radial projection technique sequence timing. After a 300-μs RF pulse and a delay of 50 μs, the signal is sampled during the readout gradient ramp-up time, resulting in a TE of 200 μs.

components of the ^{23}Na signal, as long as $[Na^+]_{ex}$ remains constant due to perfusion, and the volumes of both compartments remain constant, the measurement of Na content should be a sensitive measure of $[Na^+]_{in}$ (2).

In this work we present a 3D radial MRI technique with a UTE of 200 μs (19) that was used to characterize brain and muscular pathologies, and compared with both standard ^{23}Na Cartesian gradient-echo (GRE) sequences and standard ^{1}H MRI. Both the sequence and the reconstruction algorithm were implemented on a clinical scanner and the resulting images were sent to the picture archiving and communication system (PACS) system of the center with the rest of the examination. This was done to show that ^{23}Na MRI can be fully integrated into the clinical routine without the need for additional hardware, such as an offline image reconstruction computer. The technique was optimized for human brain tumor imaging to show its potential for routine clinical neurooncological examinations. High-grade gliomas had significantly higher Na signal than low-grade gliomas, and Na signal was generally higher within the tumor than in contralateral healthy brain tissue. We chose the Na channelopathy paramyotonia congenita (PC) as a clinical model for ^{23}Na MRI in humans because its Na channels conduct a higher amount of Na than physiological channels, which results in a myoplasmic Na accumulation associated with muscle stiffness and weakness that can be provoked by cooling and exercise. Using the ^{23}Na MRI approach, we were able to visualize acute pathologic myoplasmic Na accumulation in patients with PC after weakness was experimentally induced.

MATERIALS AND METHODS

Sequence Design

The ^{23}Na 3D radial MRI pulse sequence was implemented on a clinical whole-body scanner (1.5 T Magnetom Symphony; Siemens Medical Solutions, Erlangen, Germany) equipped with a 30 mT/m gradient system (Siemens Quantum Gradients, slew rate = 125 $Tm^{-1}s^{-1}$) and a broadband transmit/receive system suitable for ^{23}Na MRI. Images were acquired using a double-resonant (16.84 MHz/63.6 MHz) birdcage coil (Rapid Biomed GmbH, Würzburg, Germany).

A GRE pulse sequence with radial *k*-space acquisition was implemented using the manufacturer-delivered sequence development software environment (IDEA). For a given direction in *k*-space characterized by the polar angle ($0 < \theta < \pi$) and the azimuthal angle ($0 < \varphi < 2\pi$), the *x*-, *y*- and *z*-components of the readout gradient *G* were calculated according to

$$G_x = G\sin\theta\cos\varphi \quad G_y = G\sin\theta\sin\varphi \quad G_z = G\cos\theta. \quad [1]$$

A total of $N = 5000$ radial half-projections were acquired starting at the center of *k*-space (*N* being a user interface parameter that could be modified between 100 and 50000). To achieve homogeneous distribution of the data, the spherical coordinates were calculated based on an algorithm developed by Saff and Kuijaars (20), which distributes *N* points homogeneously on the surface of a sphere in a spiral manner as follows:

$$\theta_n = \arccos(h_n)\ \varphi_n = \left(\varphi_{n-1} + \frac{3.6}{\sqrt{N(1-h_n^2)}}\right) \bmod (2\pi)$$
$$\times\ h_n = -1 + \frac{2n}{N}\ \textit{with}\ n \in [1,N] \quad [2]$$

After a nonselective RF pulse with a duration of $\tau_{RF} = 300$ μs and a minimum delay of $\tau_{Delay} = 50$ μs needed to switch from transmit to receive mode, the free induction decay (FID) was sampled during the ramp-up of the readout gradient (Fig. 1). The resulting effective TE was $TE = \tau_{RF}/2 + \tau_{Delay} = 200$ μs. The signal was spoiled by using both RF spoiling (phase cycling) and gradient spoiling in the three directions (*x, y, z*), with the amplitude of the gradient spoilers modulated in the same manner as the readout gradients (Eq. [1]) to avoid any accidental refocusing of the signal.

Patient and Volunteer Studies

The study was approved by the institutional review board (IRB nos. 333/2001 and 30/2003). Written informed consent was obtained from all volunteers and patients after the nature of the examination was fully explained to them.

For comparison and localization, ^{1}H MRI was performed immediately prior to the ^{23}Na MRI protocol.

Brain Studies—Gliomas

Ten patients (age range = 38–82 years) with histologically proven low-grade ($N = 3$) and high-grade ($N = 7$) gliomas were examined. The MRI protocol consisted of a ^{23}Na 3D radial sequence (TR = 4 ms, TE = 0.2 ms, T_{acq} = 10 min, N_{acq} = 30, BW = 500 Hz/pixel, matrix size = 128 × 128 × 128, FOV = 500 mm, resulting nominal resolution $\Delta V = 4 \times 4 \times 4$ mm^3, experimentally optimized flip angle $\alpha = 15°$), a ^{1}H T_2-weighted (T_2w) fluid-attenuated inversion recovery (FLAIR) sequence (TR = 9000 ms, TE = 114 ms, T_{acq} = 3 min 38 s, slice thickness = 5 mm, BW = 130 Hz/pixel, $\alpha = 150°$), and a T_1w spin-echo (SE) sequence (TR = 400 ms, TE = 8.8 ms, T_{acq} = 1 min 10 s, slice thickness = 5 mm, BW = 115 Hz/pixel, $\alpha = 70°$). Additionally, the ^{23}Na 3D radial sequence was compared with a standard ^{23}Na 3D fast low-angle shot (FLASH) sequence (TR = 15 ms, TE = 2.69 ms, T_{acq} = 10 min 34 s, N_{acq} = 30, BW = 130 Hz/pixel, matrix size = 64 × 64, 12 slices, FOV = 500 mm, resulting nominal resolution $\Delta V = 4 \times 8 \times 10$ mm^3, $\alpha = 45°$). The flip angle α of the slice-selective RF pulse used in the ^{23}Na 3D FLASH sequence was optimized experimentally to achieve the maximum signal at $\alpha = 45°$. A 25% asymmetric readout was used to minimize the TE. Measurements were performed on two healthy volunteers and two patients (one low-grade and one high-grade glioma) in terms of the signal-to-noise ratio (SNR) and contrast-to-noise ratio (CNR).

Skeletal Muscle—PC

PC is an inherited disease of the Na^+ channels in muscle. As a result of a gating defect of the pathologic Na^+ channels, exposure to cold leads to intracellular Na^+ accumulation and muscle weakness under exercise (21). Three healthy volunteers and six patients (age range = 30–70 years) with clinically and genetically proven PC were examined. ^{23}Na MRI was performed before and after local cooling of the left lower leg for 10 min and exercising of both legs (30 knee-bends and standing on tiptoes) as described in Ref. 22. The same radial ^{23}Na MRI protocol used for the brain study was employed, and the ^{1}H MRI protocol consisted of a standard T_1-weighted SE sequence (TR = 516 ms, TE = 15 ms, matrix size = 308 × 512, slice thickness = 6 mm) and a short TI inversion recovery (STIR) sequence (TR = 5670 ms, TE = 50 ms, TI = 150 ms, matrix size = 308 × 512, slice thickness = 6 mm). In three patients the 3D radial sequence was applied twice: once with TE = 0.2 ms, and once with TE = 3 ms (in both cases TR = 15 ms). These images were subtracted to obtain a qualitative separation between the long and short T_2 components.

Image Reconstruction

To reconstruct the radially acquired data sets online, a gridding algorithm (23–25) was implemented in the standard image reconstruction environment of the scanner (ICE; Siemens Medical Solutions, Erlangen, Germany). A Kaiser-Bessel window with a width of 3.0 pixels and β = 4.2054 was used (24). To compensate for nonuniform sampling in the radial direction during gradient ramp-up, a rho-filter was implemented, which calculates the area in the cell surrounding a sample:

$$\rho_n = \frac{\pi}{N}\left\{\left(\frac{k_{n+1}}{2}\right)^2 + \left(\frac{k_n}{2}\right)^2\right\} \quad n = 0,\ldots,N-1. \qquad [3]$$

In projection imaging (PI) the sampling efficiency is optimal when the sampling density is uniform in the solid angle. According to the Nyquist criterion, the distance between adjacent samples in k-space should be less than the $FOV^{-1} = k_{max}$. To achieve isotropic 3D k-space coverage, the number of half-echo acquisitions needed for a specific resolution is (16):

$$N = 4\pi R^2, \qquad [4]$$

where R is the number of radial sampling points per projection. For $R = 64$, the number of half-echo acquisitions is $N \sim 50000$ projections. In this case a total number of $N = 5000$ projections were acquired, which implies solid angle undersampling by a factor of 10. Pipe and Menon (26,27) created an iterative numerical solution to calculate a filter for undersampled data with only the trajectory as input. Their implementation for 2D projection reconstruction yields a triangular weighting function that is constant after the trajectories exceed the Nyquist limit, and thus compensates for the correlation between data samples below the Nyquist limit, and stays constant beyond the Nyquist limit, corresponding to uncorrelated information. In this work the trajectories already exceeded the Nyquist limit at 30% of k_{max} ($n_{Nyq} = \frac{1}{2}\sqrt{\frac{N}{\pi}}$. In order to optimize density compensation, rho filters that would plateau at different points $k' = \beta k_{max}$, with $0 < \beta \leq 1$ were applied on a resolution phantom data set with $R = 64$, $N = 5000$, and $n_{Nyq} = 30$ (Fig. 2). As expected, the results showed that a filter that would plateau too early (≤20% of k_{max}) would induce image blurring, while filters that would plateau too late (≥50% of k_{max}) would strongly decrease the SNR. Density postcompensation was also tested and it resulted in an extremely low SNR.

Based on the results of the previous experiments, the spherical rho filter used for the in vivo experiments was forced to plateau at 25% of the distance to the k-space periphery k_{max} (one-fourth of the total number of sampled points R) to avoid enhancing the high-frequency data, as follows:

$$\omega_n = \begin{cases} \rho_n & 0 \leq n \leq \dfrac{N}{4} - 1 \\ \rho_{\frac{N}{4}} & \dfrac{N}{4} \leq n \leq N - 1 \end{cases}. \qquad [5]$$

After density precompensation with the rho filter, the data were regridded onto a Cartesian grid followed by a conventional 3D FFT, which yielded an isotropic data set.

Data Analysis

SNR and CNR were compared with the use of a paired t-test. Two-tailed P-values < 0.05 were considered statis-

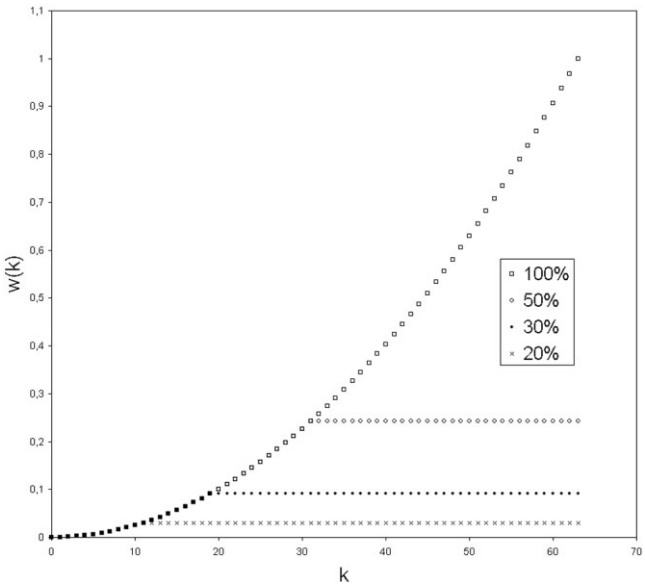

FIG. 2. Density compensation filters. The squares correspond to a full rho filter. Density compensation filters. The squares correspond to a full rho filter. The rest are set to a constant value at a given percentage of the number of sampled points.

tically significant. The measurement results for SNR and CNR are presented as the mean ± SD.

Brain Study—Gliomas

To compare the SNRs, regions of interest (ROIs) were placed in non-necrotic tumor tissue, healthy brain tissue, CSF, and vitreous humor of the ^{23}Na MR images by a radiologist and physicist in consensus. Table 1 shows a comparison of the SNR values between 3D radial and 3D Cartesian ^{23}Na MR images. To compare the SNRs of both imaging techniques, the SNR of the radial data was corrected by a factor $SNR_{Car}/SNR_{Rad} = 0.7$, reflecting the different readout bandwidth BW, TR, slice thickness, and in-plane resolution values, and calculated as $\left(\frac{SNR}{voxel}\right)_{3D} \propto \sqrt{\frac{N_{acq}N_xN_yN_zTR}{BW}}\Delta x\Delta y\Delta z$, where Nx, Ny, and Nz are the number of k-space samples in the x, y, and z-directions and $\Delta x \cdot \Delta y \cdot \Delta z$ is the voxel volume. For the Cartesian acquisition $Nx \times Ny \times Nz = 64 \times 64 \times 12$, and for the radial acquisition $Nx \times Ny \times Nz = 128 \times 128 \times 128$. In patients with low- and high-grade gliomas, the CNR between tumor tissue and white matter, and the tumor tissue signal normalized to the vitreous humor signal (S_{TT}/S_{VH}) of the ^{23}Na 3D radial images were calculated and plotted as a function of glioma grade.

Skeletal Muscle—Paramyotonia

ROIs were selected in the lower leg muscles of the ^{23}Na images and normalized to the saline reference. To evaluate the signal variation before and after cooling the left lower leg, the percentage of signal variation between the left and right legs before and after cooling was calculated as $Deviation(\%) = \frac{S_{left} - S_{right}}{S_{left}} \times 100$, where S is the mean value of the ROIs normalized to the saline reference. The percentage of signal variation of the same leg before and after cooling was calculated as $Deviation\ (\%) = \frac{S_{after} - S_{before}}{S_{before}} \times 100$.

The experimentally induced paresis was scored by a neurologist. The muscle strength before, immediately after, and 30 minutes after provocation (i.e., after the second part of the MRI examination) were scored on a six-point scale according to the grading system proposed by the British Medical Research Council (MRC): 0 = complete paralysis; 1 = minimal contraction; 2 = active movement with gravity eliminated; 3 = weak contraction against gravity; 4 = active movement against gravity and resistance; and 5 = normal strength (28). Examination of the lower limb consisted of strength testing of hip flexion, extension, abduction, and adduction; knee flexion, extension, dorsiflexion, and plantarflexion; eversion of the foot; and toe dorsiflexion and plantarflexion.

RESULTS

Brain Study—Gliomas

After the different measurement parameters were corrected with the correction factor $SNR_{Car}/SNR_{Rad} = 0.7$, the radial images had an 18% higher SNR in brain tissue ($P < 0.001$). In patients the CNR between tumor and healthy tissue was ~23% in the radial data and ~18% in the Cartesian data.

Figure 3 shows selected transverse slices through the head of a patient with a low-grade glioma (Fig. 3a–d) and a patient with a high-grade glioma (Fig. 3e–h). The tumor is seen as an area with increased signal intensity in the ^{1}H FLAIR images (Fig. 3b and f). This area corresponds well to the higher-signal-intensity regions in the ^{23}Na images (Fig. 3c and d, g and h). In the ^{1}H T_1w images (Fig. 3a and e), the tumor is seen as an area with reduced signal intensity, which corresponds best to the higher-signal-intensity regions in the ^{23}Na 3D radial images (Fig. 1d and h). The ^{23}Na images are color-coded to improve visualization.

Figure 4a shows plots of the CNR between tumor tissue and white matter, and Fig. 4b shows the tumor tissue signal normalized to the vitreous humor signal (S_{TT}/S_{VH}) in the ^{23}Na 3D radial images of patients with low- and high-grade gliomas. The CNR between tumor and healthy tissue shows a tendency to increase with glioma grade. The ratio S_{TT}/S_{VH} is lower than that for low-grade gliomas (mean ± SD = 0.8 ± 0.2) and higher than that for high-grade gliomas (mean ± SD = 1.3 ± 0.3).

Table 1
Comparison Between Cartesian and Radial Acquisition of the SNR in Various Tissues*

ROI	SNR_{CAR}	SNR_{RAD}
Vitreous humor	35.0	54.4
CSF	33.7	43.3
Brain tissue	18.5	32.4
Tumor tissue	36.7	55.3

*The SNR was measured as signal/SD.

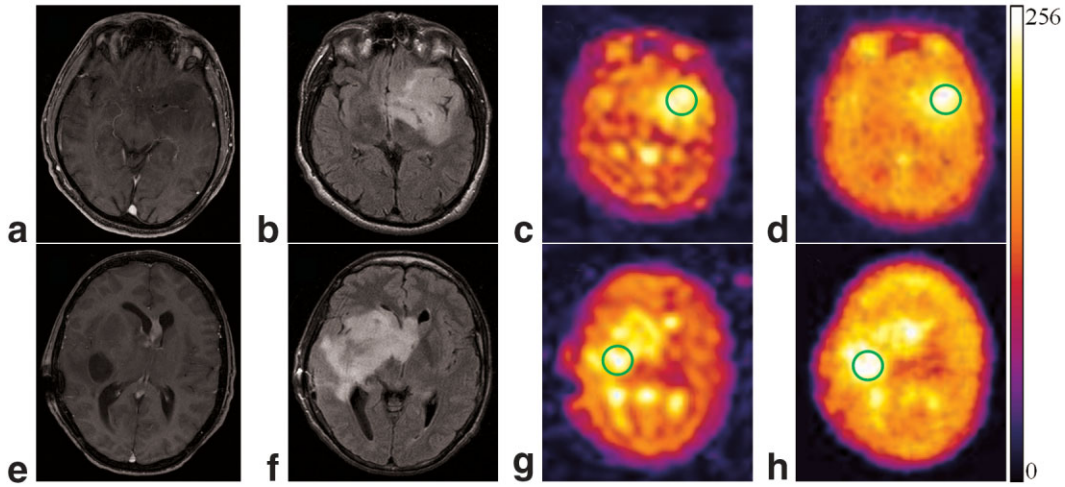

FIG. 3. Selected transverse slices through the head of a patient with a low-grade glioma (**a**–**d**) and a patient with a high-grade glioma (**e**–**h**). ^{1}H T_1w (a and e) and T_2-FLAIR (b and f) images, and ^{23}Na 3D Cartesian (c and g) and radial (d and h) images. The tumor is seen as a high-signal-intensity area in the T_2w images (b and f). These areas correspond well to the higher-signal-intensity regions in the ^{23}Na images (c and d, g and h).

Skeletal Muscle—Paramyotonia

Figure 5 shows transverse slices acquired with the 3D radial technique before and after cooling of the left lower leg. In the ^{23}Na 3D radial images acquired with the birdcage coil, regions of elevated signal are found in the upper part of the legs. This elevated signal does not relate to pathological changes, but to B_1 field inhomogeneity resulting from the proximity of the legs to the active RF coil elements caused by the tight fitting of the legs inside the coil. However, a pathological signal increase can be found when the right leg is used as reference and the ROI is positioned at the same distance from the coil (i.e., with a similar B_1 field).

In patients with PC, muscle strength prior to cooling and exercise was normal in both legs and after exercise in the noncooled leg. Hip muscle function was not influenced by cooling of the lower leg and exercise. All PC patients presented with muscle weakness in the cooled lower leg, particularly for foot and toe dorsiflexion. Muscle strength was partially recovered 45 min after cooling and exercise (MRC before: 4.9 ± 0.1; immediately after cooling: 4.2 ± 0.5; 45 min after cooling: 4.5 ± 0.3). In volunteers, muscle strength was normal under all conditions.

Table 2 shows the signal variation between the left and right legs before and after cooling for volunteers and patients as calculated in Eq. [7]. Table 3 shows the signal variation of the same leg before and after cooling for patients and volunteers according to Eq. [8]. A signal increase in the affected area of the left lower leg of about 18% (P = 0.04) was observed in the ^{23}Na images of the patients (Fig. 5f, h, and j), whereas in volunteers no significant alteration was found (~2%, P = 0.01). The difference between the right and left legs after cooling was about 21% (P = 0.006) for patients, while in volunteers no significant alteration was found (~1%, P = 0.17). Figure 5e and f were acquired with TE = 0.2 ms, and Fig. 5g and h were acquired with TE = 3 ms. In Fig. 5i and j the long-TE data are subtracted from the short-TE images. All ^{23}Na images after cooling (Fig. 5f, h, and j) showed a signal increase in the left lower leg, whereas no difference was observed in the ^{1}H images (Fig. 5a–d).

DISCUSSION

A 3D radial projection technique was implemented that allowed the acquisition of ^{23}Na MR images on a 1.5 T clinical scanner. The clinical feasibility of this technique was assessed in a pilot study in patients with low- and high-grade gliomas and in patients with PC.

As can be seen in Figs. 3 and 5, the radial images were affected by blurring. Such blurring can be caused by sub-

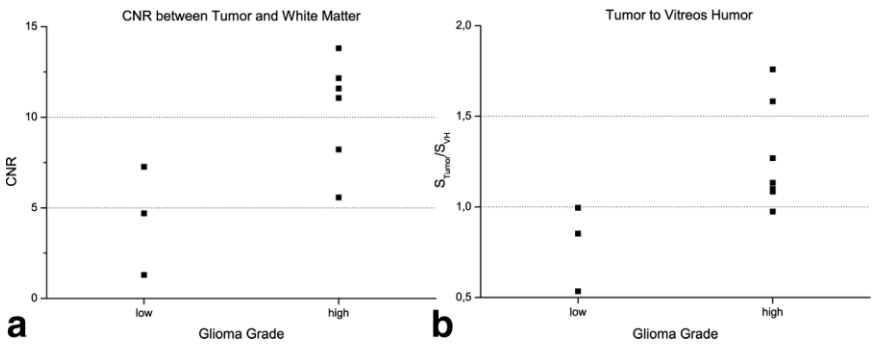

FIG. 4. Plots of the CNR between tumor tissue and contralateral white matter (**a**) and tumor tissue signal normalized to vitreous humor signal (**b**).

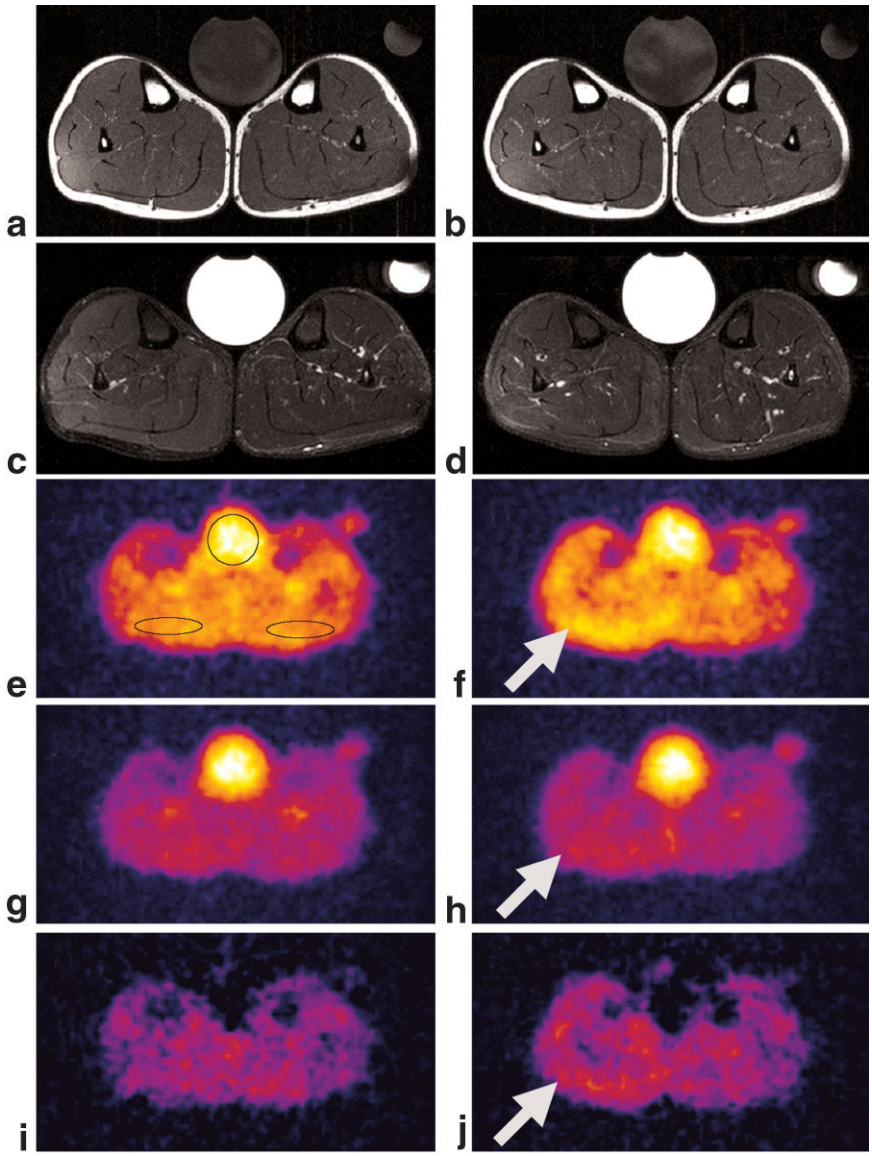

FIG. 5. ^{1}H STIR (**a**,**b**) and T_1w (**c**,**d**) images of the lower legs of a patient with PC. 3D radial images acquired before and after local cooling. Images **e** and **f** were acquired with TE = 0.2 ms, and **g** and **h** were acquired with TE = 3 ms. Images **i** and **j** correspond to the subtraction of images g and h from images e and f, respectively. All ^{23}Na images after cooling (f, h, and j) show a signal increase in the left lower leg. Two reference phantoms with NaCl are positioned between both legs and next to the right leg to determine the right and left sides and to normalize the signal intensity of the selected ROIs.

optimal filtering of the radial data before gridding, in which case a compromise between solid-angle undersampling and filter design must be achieved. A possible approach would be to increase the total number of projections N and decrease the number of averages so that the total measurement would remain the same. In this case, the Nyquist limit would be fulfilled in a larger region in k-space and the density compensation filter would not need to plateau at 0.25 k_{max}, which would probably decrease the blurring. Another source of blurring in the radial data is the decay of the short T_2 component during data acquisition (19). The Cartesian acquisition occurs after the short T_2 component of the ^{23}Na signal has already decayed, and thus does not suffer from blurring. To estimate the point spread function (PSF) in the radial images caused by the T_2 decay during data acquisition, its full width at half maximum (FWHM) for a GRE sequence can be theoretically approximated (29) to

$$FWHM_{T_2^*} = \frac{\sqrt{3}}{\pi}\left(\frac{T_s}{T_2^*}\right)\Delta x, \qquad [9]$$

Table 2
Comparison Between ROIs of the Left and Right Lower Leg Normalized to the Saline Reference Before and After Cooling for Volunteers and Patients*

% (mean ± SD)	Before cooling	After cooling
Volunteers	1.1 ± 1.1	0.8 ± 0.7
Patients	4.0 ± 1.8	21.4 ± 2.7

*Normalized as $Deviation(\%) = \frac{S_{left} - S_{right}}{S_{left}} \times 100$

Table 3
Comparison Between ROIs of the Same Leg Normalized to the Saline Reference Before and After Cooling for Volunteers and Patients*

% (mean ± SD)	Right	Left (cooled)
Volunteers	3.3 ± 1.5	1.9 ± 0.5
Patients	6.3 ± 2.1	18.0 ± 8.3

*Normalized as $Deviation\ (\%) = \frac{S_{after} - S_{before}}{S_{before}} \times 100$

which for a T_S = 2000 μs and T_2 = 500 μs results in $FWHM_{T2^*}$ = 2.2 Δx. Two solutions are available to minimize this blurring effect. First, the readout bandwidth can be increased. Due to gradient limitations, a readout BW of 500 Hz/pixel cannot be exceeded. Second, it is possible to apply a correction filter to the radial data during image reconstruction that would compensate for the T_2 decay. However, this would imply that the biexponential T_2 decay times in vivo are accurately known, which is not the case. Furthermore, the SNR of the images would decrease and in voxels without biexponential decay the filter would fail. An approximately twofold decrease of spatial resolution is therefore to be expected in radial ^{23}Na data sets with short TE.

^{23}Na MRI shows increased ^{23}Na signal in tumors relative to healthy brain tissue. Our preliminary results obtained in 10 patients indicate that Na^+ content is lower in low-grade gliomas in vitreous humor, and is higher in high-grade gliomas than in vitreous humor ([Na^+] has been measured to be ~150 mM in vitreous humor (30)). However, more patient studies are required to confirm this tendency. In comparison with the standard Cartesian images (TE = 2.69 ms), the radially acquired images (TE = 0.2 ms) show an 18% increase in SNR in healthy volunteers. While the higher-signal-intensity regions of the ^{23}Na Cartesian images seem to correspond well with the increased-signal-intensity regions of the ^{1}H FLAIR images, the higher-signal-intensity regions of the ^{23}Na radial images apparently correspond better to the low-signal-intensity regions of the ^{1}H T_1w images. These results can be explained by the approximately 10-fold shorter TE of the radial technique compared to the Cartesian technique, which allows for the acquisition of the total Na signal (i.e., long and short T_2 components) (16) and therefore the total Na^+ content, including the total Na^+ tissue and blood contents. The Cartesian technique detects partial Na^+ tissue content and total blood Na^+ content. The SNR increase in radial compared to Cartesian techniques is only 18% because there is edema in the tumor region. On the other hand, the radial images are able to delineate the tumor region more accurately because they actually detect the total Na^+ content in tissue. However, the value of these techniques does not lie in their ability to depict tumors, but rather in their potential to quantify the Na+ content and hence provide information about tissue viability, as shown in Ref. 31. With the use of quantitative techniques, ^{23}Na MRI may provide early noninvasive information about tumor therapy response and may help to differentiate radiation necrosis from recurrent tumor tissue before morphological changes can be observed. In combination with ^{1}H MRI protocols, it may provide additional functional information and improve the diagnostic specificity of multiparametric analysis methods.

In patients with PC, ^{23}Na MRI with short TE visualized Na accumulation that was associated with muscle weakness. Considering the fact that the ^{1}H T_2w images did not show an increase in extracellular space due to edema, the increase in ^{23}Na signal appears to be related to an increase in $[Na]_{in}$. Assuming that Fig. 4g and h relate mainly to the long T_2 component, and Fig. 4i and j relate mainly to the short T_2 component, one can conclude that the accumulation of intracellular ^{23}Na after cooling leads to an increase in the concentration of both T_2 components.

Because of its ability to detect changes in Na+ content noninvasively, ^{23}Na MRI may be a useful tool for researching muscle channelopathies whose processes are still not fully described. Furthermore, the volumetric capabilities of ^{23}Na MRI can provide information that does not have the physical limitations of a biopsy (i.e., one sample from a highly heterogeneous volume), which currently is the standard method to assess muscular Na+ concentration levels (6).

To perform a quantitative evaluation of the Na content in a ^{23}Na MRI study, the effects of T_1 and T_2 relaxation and field inhomogeneity must be accounted for during data acquisition or postprocessing. Although it would have been possible to acquire coil field maps to correct the signal intensity of the Na images, the acquisition scheme used in this study was inadequate for quantitation of the total Na signal. For a quantitative evaluation the TR must be larger than five times the T_1 to ensure full relaxation of the signal during data acquisition. With TE = 0.2 ms and TR = 4 ms, the 3D radial sequence could not provide quantitative results. A $TR \gg 5 \times T_1$ would have prolonged the measurement time by a factor of 25, which is clinically unfeasible. One technique that allows for such long TRs (on the order of 100 ms), as well as UTEs, is TPI. In this method the TR is inherently longer due to the long readout duration, and the sampling efficiency results in acceptable measurement times (~10 min) similar to those achieved in this study. Therefore, TPI would be more adequate for quantitation. A comparison of TPI and PI should be the subject of future research.

Although the radial sequence used in this study did not deliver quantitative results, the results show that the partially saturated signal may be a useful qualitative marker of disease. To evaluate the effect of T_1 saturation on the different Na compartments, we calculated the signal difference expected using the radial sequence implemented in this study (TR = 4 ms, TE = 0.2 ms) between a phantom containing 0.3% NaCl (T_1 = 50 ms, T_2 = 40 ms) and a phantom containing 0.3% NaCl + 4% agarose (T_1 = 23 ms, T_{2fast} = 0.3, T_{2slow} = 18 ms, M_{fast} = 0.6, M_{slow} = 0.4). Using the FLASH sequence formula (32), the agarose phantom signal is expected to be 1.6 times higher than the saline phantom signal. This expected signal difference was observed in a phantom experiment using the phantoms described above. Therefore, if measurements of T_1 for the fluid compartments within the tissue could be accurately measured, it is possible that the differences in T_1 between the tissue and fluid compartments could be used to weight the signal toward its nontrivial components (i.e., excluding edema, CSF, etc.).

In conclusion, a ^{23}Na 3D radial MRI clinical protocol was developed and tested in patients with cerebral gliomas and PC. ^{23}Na 3D radial MRI visualized Na accumulation and provided diagnostically useful information for both clinical groups within clinically acceptable measurement times of about 10 min at 1.5 T. Higher field strengths may allow ^{23}Na MRI to become a clinically relevant application that can lead to higher SNR or shorter measurement times by reducing signal averaging. ^{23}Na MRI has been integrated into clinical work-ups, and has the potential to

evolve from a research topic to a clinically feasible diagnostic tool.

ACKNOWLEDGMENTS

The authors thank Drs. Renate Jerecic and Ioannis Panagiotelis for stimulating discussions, and Drs. Sven Zuehlsdorff, Andrew Larson, and Achim Bankamp for support with the software development.

REFERENCES

1. Hilal SK, Ra JB, Oh CH, Mun IK, Einstein SG, Roschmann P. Sodium imaging. In: Stark DD, Bradley WG, editors. Magnetic resonance imaging. St. Louis: C.V. Mosby; 1988. p 715–729.
2. Owerkerk R, Bleich KB, Gillen JS, Pomper MG, Bottomley PA. Tissue sodium concentration in human brain tumors as measured with ^{23}Na MR imaging. Radiology 2003;227:529–537.
3. Kim RJ, Judd RM, Chen EL, Fieno DS, Parrish TB, Lima JAC. Relationship of elevated ^{23}Na magnetic resonance image intensity to infarct size after acute reperfused myocardial infarction. Circulation 1999;100: 185–192.
4. Constantinides CD, Kraitchman DL, O'Brien KO, Boada FE, Gillen J, Bottomley PA. Noninvasive quantification of total sodium concentrations in acute reperfused myocardial infarction using ^{23}Na MRI. Magn Reson Med 2001;46:1144–1151.
5. Kushnir T, Knubovets T, Itzchak Y, Eliav U, Sadeh M, Rapoport L, Kott E, Navon G. In vivo ^{23}Na NMR studies of myotonic dystrophy. Magn Reson Med 1997;37:192–196.
6. Constantinides CD, Gillen JS, Boada FE, Pomper MG, Bottomley PA. Human skeletal muscle: sodium MR imaging and quantification—potential applications in exercise and disease. Radiology 2000;216:559–568.
7. Pekar J, Leigh JS. Detection of bi-exponential relaxation in sodium-23 facilitated by double quantum filtering. J Magn Reson 1986;69:582–584.
8. Jaccard G, Wimperis S, Bodenhausen G. Multiple quantum NMR spectroscopy of S-3/2 spins in isotropic phase: a new probe for multiexponential relaxation. J Chem Phys 1986;85:6282–6293.
9. Rooney WD, Springer Jr CS. A comprehensive approach to the analysis and interpretation of the resonances of spins 3/2 from living systems. NMR Biomed 1991;4:209–226.
10. Rooney WD, Springer Jr CS. The molecular environment of intracellular sodium: ^{23}Na NMR relaxation. NMR Biomed 1991;4:227–245.
11. Springer CS. Biological systems: spin-3/2 nuclei. In: Grant DM, Harris RK, editors. Encyclopedia of nuclear magnetic resonance. New York: John Wiley & Sons, 1996. p 940–951.
12. Parrish TB, Fieno DS, Fitzerald SW, Judd RM. Theoretical basis for sodium and potassium MRI of the human heart at 1.5T. Magn Reson Med 1997;38:653–661.
13. Narayana PA, Kulkarni MV, Mehta SD. NMR of ^{23}Na in biological systems. In: Partain CL, Price RR, Patton JA, Kulkarni MV, James AE, editors. Magnetic resonance imaging physical principles and instrumentation. 2nd ed. Philadelphia: W.B. Saunders; 1988. p 1553–1563.
14. Van Emous JG, Vleggeert-Lankamp CL, Nederhoff MG, Ruigrok TJ, Van Echteld CJ. Postischemic Na(+)-K(+)-ATPase reactivation is delayed in the absence of glycolytic ATP in isolated rat hearts. Am J Physiol Heart Circ Physiol 2001;280:H2189– H2195.
15. Borthakur A, Hancu I, Boada FE, Shen GX, Shapiro EM, Reddy R. In vivo triple quantum filtered twisted projection sodium MRI of human articular cartilage. J Magn Reson 1999;141:286–290.
16. Boada FE, Christensen JD, Gillen JS, Thulborn KR. Three-dimensional projection imaging with half the number of projections. Magn Reson Med 1997;37:470–477.
17. Boada FE, Gillen JS, Shen GX, Chang SY, Thulborn KR. Fast three dimensional sodium imaging. Magn Reson Med 1997;37:706–715.
18. Boada FE, Shen GX, Chang SY, Thulborn KR. Spectrally weighted twisted projection imaging: reducing T_2 signal attenuation effects in fast three dimensional sodium imaging. Magn Reson Med 1997;38: 1022–1028.
19. Jerecic R, Bock M, Nielles-Vallespin S, Wacker C, Bauer W, Schad LR. ECG-gated ^{23}Na-MRI of the human heart using a 3D-radial projection technique with ultrashort echo times. MAGMA 2004;16:297–302.
20. Saff EB, Kuijaars ABJ. Distributing many points on a sphere. Math Intell 1997;19.1:5–11.
21. Lehmann-Horn F, Jurkat-Rott K. Voltage-gated ion channels and hereditary disease. Physiol Rev 1999;79:1317–1371.
22. Nielles-Vallespin S, Weber MA, Huttner H, Bankamp A, Bock M, Woehrle J, Meinck HM, Schad LR. Comparison of Cartesian and radial ^{23}Na MRI for visualization of intracellular sodium accumulation in patients with a muscular ^{23}Na channelopathy. In: Proceedings of the 13th Annual Meeting of ISMRM, Miami Beach, FL, USA, 2005 (Abstract 2566).
23. O'Sullivan J. A fast sinc function gridding algorithm for Fourier inversion in computer tomography. IEEE Trans Med Imaging 1985;4:200–207.
24. Jackson J, Meyer C, Nishimura D, Macovski A. Selection of a convolution function for Fourier inversion using gridding. IEEE Trans Med Imaging 1991;MI-10:473–478.
25. Schomberg H, Timmer J. The gridding method for image reconstruction by Fourier transformation. IEEE Trans Med Imaging 1995;14:596–607.
26. Pipe JG, Menon P. Sampling density compensation in MRI: Rationale and an iterative numerical solution. Magn Reson Med 1999;41:179–186.
27. Pipe JG. Reconstructing MR images from undersampled data: data-weighting considerations. Magn Reson Med 2000;43:867–875.
28. Victor M, Ropper AH. Adams and Victor's principles of neurology. 7th ed. New York, PA: McGraw-Hill Inc.; 2001. p 1464–1479.
29. Haacke EM, Brown RW, Thompson MR, Venkatesan R. Magnetic resonance imaging: physical principles and sequence design. New York: John Wiley and Sons; 1999.
30. McNeil AR, Gardner A, Stables S. Simple method for improving the precision of electrolyte measurements in vitreous humor. Clin Chem 1999;45:135–136.
31. Boada FE, LaVerde G, Jungreis C, Nemoto E, Tanase C, Hancu I. Loss of cell ion homeostasis and cell viability in the brain: what sodium MRI can tell us. Curr Top Dev Biol 2005;70:77–101.
32. Haase A, Frahm J, Matthaei D, Haenicke W, Merboldt KD. FLASH imaging. Rapid NMR imaging using low flip-angle pulses. J Magn Reson 1986;67:258–266.